Ab initio calculation of electron–phonon coupling in monoclinic β-Ga2O3 crystal

Krishnendu Ghosh and Uttam Singisetti

Articles you may be interested in

Electron-phonon couplings and carrier mobility in graphynes sheet calculated using the Wannier-interpolation approach
J. Chem. Phys. **141**, 034704 (2014); 10.1063/1.4887538

Electron-phonon superconductivity in LaO0.5F0.5BiSe2
J. Appl. Phys. **115**, 233901 (2014); 10.1063/1.4883755

Orbital dependent Rashba splitting and electron-phonon coupling of 2D Bi phase on Cu(100) surface
J. Chem. Phys. **139**, 184707 (2013); 10.1063/1.4828865

Theoretical examination of superconductivity in the cubic antiperovskite Cr3GaN under pressure
J. Appl. Phys. **114**, 053905 (2013); 10.1063/1.4817072

Incorporation, valence state, and electronic structure of Mn and Cr in bulk single crystal β–Ga2O3
J. Appl. Phys. **111**, 123716 (2012); 10.1063/1.4729289

Ab initio calculation of electron–phonon coupling in monoclinic *β*-Ga₂O₃ crystal

Krishnendu Ghosh[a)] and Uttam Singisetti[b)]

Electrical Engineering Department, University at Buffalo, Buffalo, New York 14260, USA

The interaction between electrons and vibrational modes in monoclinic *β*-Ga₂O₃ is theoretically investigated using *ab-initio* calculations. The large primitive cell of *β*-Ga₂O₃ gives rise to 30 phonon modes all of which are taken into account in transport calculation. The electron-phonon interaction is calculated under density functional perturbation theory and then interpolated using Wannier–Fourier interpolation. The long-range interaction elements between electrons and polar optical phonon (POP) modes are calculated separately using the Born effective charge tensor. The direction dependence of the long-range POP coupling in a monoclinic crystal is explored and is included in the transport calculations. Scattering rate calculations are done using the Fermi golden rule followed by solving the Boltzmann transport equation using the Rode's method to estimate low field mobility. A room temperature mobility of $115 \, \text{cm}^2/\text{V s}$ is observed. Comparison with recent experimentally reported mobility is done for a wide range of temperatures (30 K–650 K). It is also found that the POP interaction dominates the electron mobility under low electric field conditions. The relative contribution of the different POP modes is analyzed and the mode $21 \, \text{meV}$ POP is found to have the highest impact on low field electron mobility at room temperature. *Published by AIP Publishing.* [http://dx.doi.org/10.1063/1.4961308]

Recently, *β*-Ga₂O₃ has emerged as an extremely promising candidate for power electronics due to its large bandgap (4.9 eV) and experimental demonstration of *β*-Ga₂O₃ transistors with very high breakdown voltage (∼750 V).[1–4] Apart from transistors, Schottky barrier diodes based on this material have also been demonstrated.[5–7] A well-developed bulk and epitaxial crystal growth technology further provides cost advantages.[1–4] It is crucial to have a thorough understanding of the electron transport properties to get an insight into the device operation and also optimize the performance. Although there have been several studies on the electronic structure[8–11] and dielectric properties[12,13] of the material, only a few reports[14,15] are available on carrier transport in the material. Unlike the traditional semiconductors, *β*-Ga₂O₃ has a highly anisotropic monoclinic base centered crystal (C2/m space group) structure with 10 atoms in the primitive cell.[10] This leads to the large number of phonon modes (30 modes) in the material which makes it complex to analyze the interaction between electrons and phonons that plays a pivotal role in determining mobility. The low symmetry of the crystal poses question on the anisotropy of carrier transport. Though an early experiment showed anisotropic carrier mobility,[16] later on it was found that the low field mobility is actually isotropic.[15] Also, given the presence of both non-polar and polar interactions between the electrons and the phonons, it is critical to evaluate which type would dominate electron transport in *β*-Ga₂O₃. Conventional non-polar scattering rate equations require deformation potentials (DPs) which are usually found out empirically while polar scattering rates require knowledge of relative contribution of the phonon modes to the dielectric constant. None of these are well established theoretically or experimentally for *β*-Ga₂O₃. A recent work[15] on low field transport reported the dominant optical phonon mode from empirical fitting of experimental data; however, they did not consider all the phonon modes in the calculation. In this work, we theoretically study the low field electron transport in *β*-Ga₂O₃ from first principles taking into account all the phonon modes. The dominant phonon mode limiting the low field mobility is identified.

First, we carry out the standard density functional theory (DFT) calculation on a *β*-Ga₂O₃ primitive cell which contains 4 Ga atoms and 6 O atoms using the *ab initio* package Quantum ESPRESSO (QE).[17] The real space lattice and the Brillouin zone (BZ) are visualized by XCrySDen[18] and are shown in Figs. 1(a) and 1(b), respectively, with the BZ showing the high symmetry points identified as black dots. The reciprocal vectors are also shown. The details about the DFT calculation are given in the supplementary material. The calculated energy eigen values are interpolated using maximally localized Wannier (MLW) functions.[19] For low field transport, we are interested only with the first conduction band which is dominated by Ga 4s orbital.[9] The Wannier interpolated first conduction band matches well with previously reported calculations (see Fig. S1).

After obtaining the electronic energy dispersion, we focus on finding out the lattice response under the density functional perturbation theory (DFPT) formalism[20] using QE. The details of this calculation are again given in the supplementary material. The dynamical matrices (D_q) and the perturbation in the self-consistent potential are calculated for phonon wave-vectors (we refer this as q points) on a coarse mesh. Next, a Fourier interpolation is done to obtain the eigen values at intermediate q points. The resulting phonon spectrum is shown in Fig. 2(a), which shows the phonon modes dispersion along the three reciprocal vector directions.

a)Email: kghosh3@buffalo.edu. Tel.: 716-645-1017.
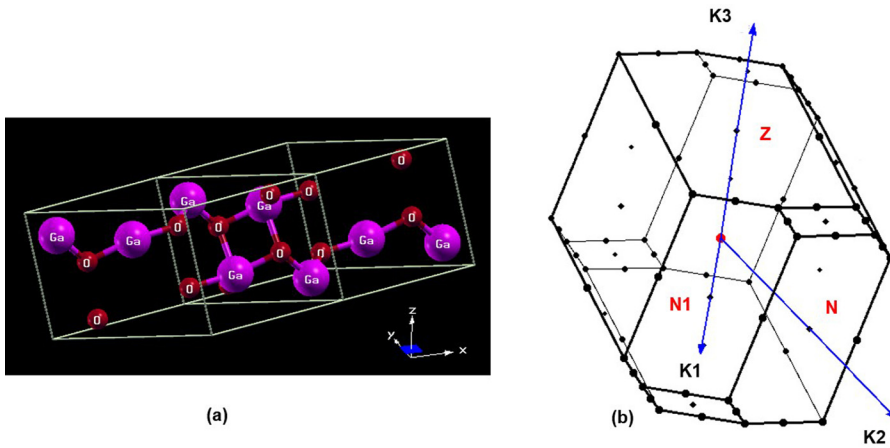b)Email: uttamsin@buffalo.edu. Tel.: 716-645-1536. Fax: 716-645-3656.

FIG. 1. (a) The real-space lattice of monoclinic β-Ga$_2$O$_3$ crystal. (b) The Brillouin zone of the crystal with the high symmetry points being noted by the dotted points, the red dot at the center is the Γ point, and the blue lines show the reciprocal lattice vectors.

It shows the 30 phonon modes arising from the 10 atoms in the primitive cell. An important point to note here is that the phonon modes shown in Fig. 2(a) do not take into account the contribution from the macroscopic field due to presence of effective polarization charges on the atoms. The long–range interaction arising from this macroscopic field is calculated separately in the next paragraph. In the following paragraph, we discuss the electron-phonon interaction elements in β-Ga$_2$O$_3$.

The interaction elements for the νth phonon mode is given by $M_q^\nu = \left\langle \psi_{k+q} \left| \frac{\partial V_{scf}}{\partial q} \right| \psi_k \right\rangle$, where $\frac{\partial V_{scf}}{\partial q}$ is the perturbation in the self-consistent potential (V_{scf}) due to phonon wave-vector q and ψ_k is the electronic wave-function. These interaction elements are calculated on the coarse mesh first. However, transport calculations need very fine resolution of the matrix elements in order to achieve convergence in scattering rates. The coarse mesh matrix elements are interpolated on to a fine mesh using a Wannier–Fourier (WF) interpolation[21] scheme (Electron–Phonon Wannier (EPW)) utilizing the crystal periodicity. However, as pointed out in

the literature,[22,23] the polar interactions between electrons and the polar optical phonon (POP) modes due to a macroscopic electric field should be treated separately due to the long range nature of the polar interaction. Hence, we treat the long-range POP contribution separately. First, we calculate the electron–POP interaction on the coarse mesh by the method described by Verdi.[23] The Born effective charge tensor and the dielectric constant are calculated by DFPT for $q = 0$. The electron-POP interaction are calculated on the coarse q-mesh using Eq. (4) of Ref. 23. These elements are subtracted from the DFPT calculated matrix elements on the coarse mesh. This leaves us with the short range (cell-periodic part; both non-polar optical and acoustic interactions) part of the interaction on the coarse mesh. Next, we carry out the WF scheme to find out the matrix elements on a fine mesh. The real-space formulation needed for the interpolation is described in the supplementary material. Apart from interpolating the electron–phonon matrix elements, the WF scheme also interpolates the phonon dynamical matrices and hence we could obtain the phonon displacement vectors and
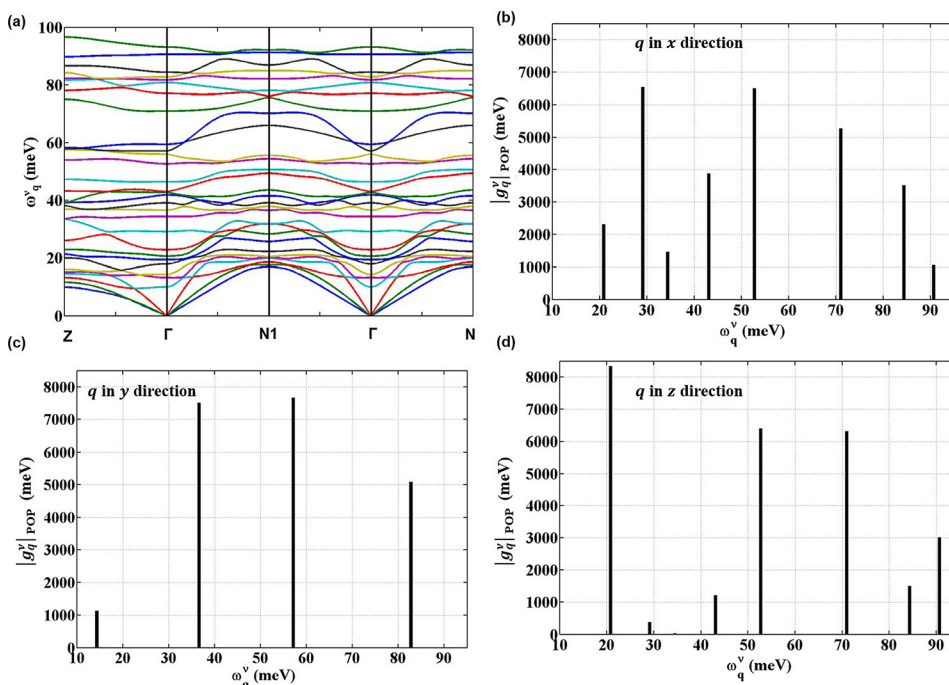

FIG. 2. (a) The phonon dispersions calculated by DFPT and interpolated through Fourier interpolation. The dispersion is shown only along the three reciprocal lattice vectors. (b)–(d) The long-range coupling elements in three Cartesian directions. The coupling elements follow a similar trend to that of the dipole strength shown in the supplementary material.

eigen values on a fine mesh. These are used to recalculate the electron POP interaction elements on the fine mesh using the same the method described in Ref. 23. It is important to note here is the fact that we use two different fine q-meshes for long range (POP) and short range matrix elements to facilitate our transport calculation. The long range elements (POP) are calculated on a $40 \times 40 \times 40$ uniform mesh covering 0.2 times the length of the reciprocal vectors in each direction surrounding the Γ point while the short range elements are calculated on a similar $40 \times 40 \times 40$ uniform mesh 0.6 times the length of the reciprocal vectors. This choice of meshes ensures accuracy in the long-range elements (since they decay fast near the Γ point) without demanding excessive memory for computation.

Figures 2 (b)–2(d) show the calculated electron-phonon long–range (POP) coupling strength $\left(g_q^\nu = \sqrt{\frac{\hbar}{2\omega_q^\nu}} M_q^\nu \right)$, in three different Cartesian directions in the BZ, ω_q^ν is the phonon mode frequency and $\hbar$ is the reduced Planck's constant, M_q^ν is described before, and the mass factor of the quantized vibrational amplitude is actually taken care of within M_q^ν. It is observed that the coupling strengths are direction dependent, with different modes having strong strengths in different directions. This will play an important role in mobility calculations. There are several significantly strong coupling strengths that could be observed, for example, 53 meV and 71 meV (x and z directions), 39 meV and 56 meV (y direction), 21 meV (in z direction) and 29 meV (in x direction). The polar coupling strength of a mode in a given direction is due to the projection of the net dipole strength along that direction (since polar coupling is the dot product of dipole strength and q vector). A discussion on effective dipole strength in different directions (along with LO–TO splitting) and comparison of corresponding infra-red (IR) strength are given in the supplementary material. The most important information evident from the direction dependent POP coupling elements is the fact that the B_u modes, polarized only in the x-z plane, have different coupling strength in x and z directions which is also evident from the direction dependent LO–TO splitting shown in Table SI. On the other hand, the A_u modes are polarized only in the y direction. Hence, one must be careful while carrying out transport calculations since the conventional way of considering a spherical average in the q-space is not a good approximation in this case. Another important issue to consider is the screening of the vibrational modes. We take care of screening by the fact that higher energy modes can efficiently screen the low energy modes. Note that this screening is taken care of for short range modes automatically since the short rage matrix elements follow the self-consistent potential. However, we need to treat this screening separately for the POP. Here, we include the screening by using a frequency dependent dielectric constant based on Lyddane–Sachs–Teller (LST) theory[24] (see the supplementary material for more details).

Next, we calculate the electron scattering rates under Fermi golden rule. As discussed previously, we need to consider direction dependent matrix elements and hence the conventional way of carrying out the q-space integration with spherical symmetry is not a good choice. Here, the q-space

integration is performed numerically using a Gaussian smearing of the energy conserving delta function, which is a common practice in numerical BZ integrations.[25] The resulting scattering rates are shown in Figs. 3(a) and 3(b). Fig. 3(a) shows the three main different scattering mechanisms that affect the electron transport. The POP scattering rate clearly shows the onset of the emission of the dominant POP mode near 21 meV. The non-polar scattering is a result of combined deformation potential (DP) interaction with acoustic and non-polar optical phonons. It is noted that we calculate the ionized impurity (II) scattering rate using a simple Brooks Herring model[26] with a static Debye like screening. An n-type doping of $1.1 \times 10^{17}\,\mathrm{cm}^{-3}$ and an effective mass of 0.3 times free electron mass is taken for the calculation. Incomplete ionization of the dopants at low temperature is taken into account with a dopant activation energy of 31 meV.[7] Fig. 3(a) also shows the anti-symmetric part of the electronic distribution function obtained after solving the Boltzmann Transport Equation (BTE) through iteration which is discussed later.

Fig. 3(b) shows the individual contribution of the POP modes to the scattering rate. There are several factors, namely, the coupling strength (g_q^ν), energy of the interacting electron (E_k), and the temperature, which control which mode will dominate in determining the low-field mobility. We discuss the role of each of these factors here and show
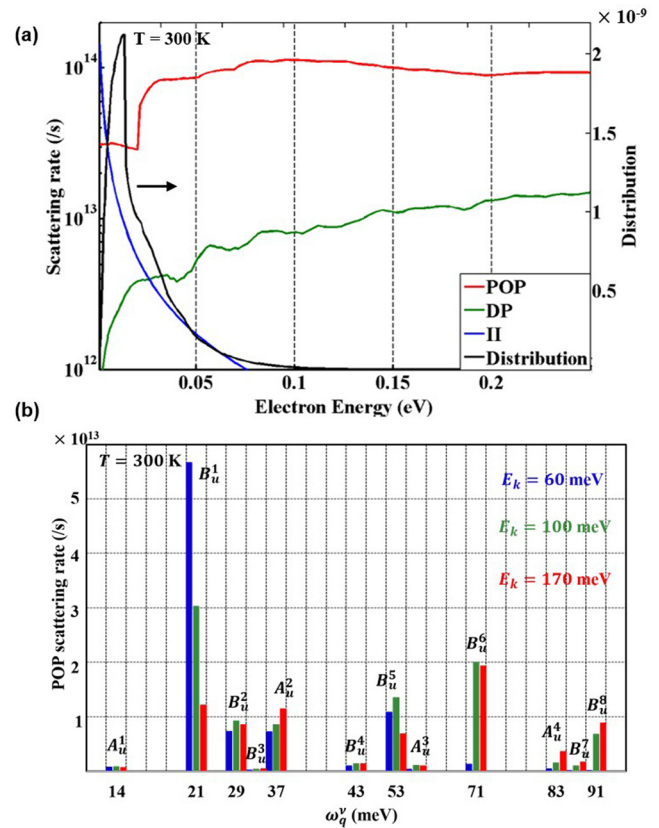

FIG. 3. (a) The red, green, and blue curves show the scattering rates originating from the three mechanisms—POP, DP, and II, respectively, at room temperature. Clearly, the POP mechanism dominates the other two and also the sharp turn on the emission of the dominant POP mode around 21 meV is observed. The right y-axis shows the calculated low-field anti symmetric electron distribution function (black curve) using Rode's method. (b) The calculated scattering strength of different POP phonon modes for three different electron energies.

how different modes could become important at different regimes of transport. The coupling strength of a mode has been discussed in detail before. The role of electron energy (E_k) comes in the form of available density of states after the scattering occurs. To clarify further, scattering rate due to a phonon mode with higher coupling strength could be suppressed if the available electronic density of states after emission (or absorption) of that mode is low. So under low electric field conditions, when the anti-symmetric electron distribution is close to the Γ point (see Fig. 3(a), emission of a high energy phonon mode is unlikely even though the coupling strength of that mode is high. Finally, the temperature influences the interaction via the Bose-Einstein occupation statistics which is common to all forms of phonon scattering. A higher temperature will increase the occupation of both low and high energy phonon modes and hence the POP modes at higher energies would also start to affect the electron transport.

The three bar plots in Fig. 3(b) show the electronic scattering rate due to POP interaction for three different electron energies. We see that the most dominant phonon mode for a low energy electron ($E_k \approx 60\,meV$) is 21 meV. As shown in Fig. 3(a), in low field conditions the electron distribution dies off quickly with energy, hence low energy electrons determine the mobility. On the other hand, for relatively higher energy electrons ($E_k \approx 170\,meV$) the dominant phonon mode is at 71 meV. This is due to the fact that although the emission of a 71 meV phonon by a 60 meV electron is prohibited, the same by a 170 meV electron is feasible. This trade-off between the phonon mode and the electronic kinetic energy is what makes the electron–polar mode interaction interesting in crystals with multiple LO modes. Hence, as we can see that different modes could affect the electron transport based on the electron energy, it is difficult to specify a mode that will determine the transport across the entire temperature and transport regime. However, for analyzing low-field transport using the Frölich model for POP scattering, a POP mode with energy around 21 meV will give approximate scattering rates based on the calculations discussed above. Hence, majority of the electrons will interact with the 21 meV mode. It is noted that a non-polar phonon of 30 meV was shown to be the dominant mode in Ref. 15, similar low energy phonon mode is also seen here for room temperature mobility. However, Ref. 15 did not consider POP scattering due to the low energy phonons, instead an empirical deformation potential was used to fit the experimental data.

We use Rode's method[27,28] to iteratively solve the BTE which takes into account the inelastic nature of POP scattering. Here, we would like to mention that impurity scattering entered the BTE under the well-known relaxation time approximation (RTA). Fig. 4 shows the calculated net mobility as a function of temperature. We find that at low temperature (30 K–80 K) the mobility shows a brief increasing trend which is due to the II scattering dominated transport. As the temperature is further increased, the POP scattering plays the dominant role and the mobility starts dropping. At room temperature, the estimated mobility is around 115 cm²/V s. We also show the mobility data from recent experimental study by Parisini *et al*. Good agreement between our calculation
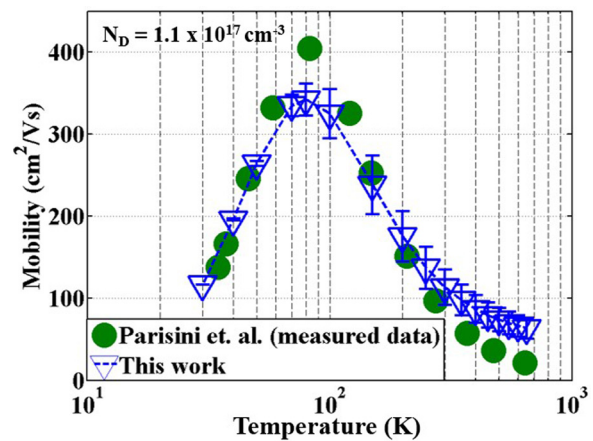

FIG. 4. The calculated mobility (blue open triangles) for a wide temperature range (30 K–650 K). For comparison, recently reported experimental data (green closed circles) is shown. The experimental drift mobility data in Ref. 15, which is used here for comparison, is obtained by taking into account the Hall correction factor of the measured Hall mobility on bulk Ga_2O_3 crystals.[15] The error bars are calculated assuming 10% accuracy in the dielectric constant and short-range matrix elements.

and the experimental data could be observed for a wide range of temperature (30 K–650 K).

In conclusion, we have theoretically investigated the electron-phonon interaction in β-Ga_2O_3 from first principles. Low field mobility values are predicted for a varying range of temperature. The interesting physics of electron POP interaction is explored for multi-phonon semiconductors. The polarization of the phonon mode, the electron energy, and the temperature play a crucial role in determining which phonon modes limit the electron transport. At room temperature, POP mode with energy of 21 meV limits the low field mobility.

See supplementary material for descriptions of DFT, DFPT, and electron–phonon calculations, details on dipole oscillation and dielectric tensor, Wannier representations needed for interpolation, and high temperature effects on POP scattering rates.

[1]M. Higashiwaki, K. Sasaki, M. H. Wong, T. Kamimura, D. Krishnamurthy, A. Kuramata, T. Masui, and S. Yamakoshi, "Depletion-mode Ga_2O_3 MOSFETs on beta-Ga_2O_3 (010) substrates with Si-ion-implanted channel and contacts," Tech. Dig. - IEEE Int. Electron Devices Meet. 2013, 28.7.1.
[2]M. Higashiwaki, K. Sasaki, T. Kamimura, M. Hoi Wong, D. Krishnamurthy, A. Kuramata, T. Masui, and S. Yamakoshi, "Depletion-mode Ga_2O_3 metal-oxide-semiconductor field-effect transistors on β-Ga_2O_3 (010) substrates and temperature dependence of their device characteristics," Appl. Phys. Lett. **103**, 123511 (2013).
[3]M. Higashiwaki, K. Sasaki, A. Kuramata, T. Masui, and S. Yamakoshi, "Gallium oxide (Ga_2O_3) metal-semiconductor field-effect transistors on single-crystal β-Ga_2O_3 (010) substrates," Appl. Phys. Lett. **100**, 013504 (2012).
[4]M. Higashiwaki, K. Sasaki, H. Murakami, Y. Kumagai, A. Koukitu, A. Kuramata, T. Masui, and S. Yamakoshi, "Recent progress in Ga_2O_3 power devices," Semicond. Sci. Technol. **31**, 034001 (2016).

[5]K. Sasaki, M. Higashiwaki, A. Kuramata, T. Masui, and S. Yamakoshi, "Ga$_2$O$_3$ Schottky barrier diodes fabricated by using single-crystal β-Ga$_2$O$_3$ (010) substrates," IEEE Electron Device Lett. **34**, 493 (2013).

[6]M. Higashiwaki, "Ga$_2$O$_3$ schottky barrier diodes with n-Ga$_2$O$_3$ drift layers grown by HVPE," in *IEEE Device Research Conference* (2015), pp. 29–30.

[7]T. Oishi, Y. Koga, K. Harada, and M. Kasu, "High-mobility β-Ga$_2$O$_3$($\bar{2}$01) single crystals grown by edge-defined film-fed growth method and their Schottky barrier diodes with Ni contact," Appl. Phys. Express **8**, 031101 (2015).

[8]H. He, R. Orlando, M. A. Blanco, R. Pandey, E. Amzallag, I. Baraille, and M. Rérat, "First-principles study of the structural, electronic, and optical properties of Ga$_2$O$_3$ in its monoclinic and hexagonal phases," Phys. Rev. B **74**, 195123 (2006).

[9]Y. Zhang, J. Yan, G. Zhao, and W. Xie, "First-principles study on electronic structure and optical properties of Sn-doped β-Ga$_2$O$_3$," Phys. B: Condens. Matter **405**, 3899–3903 (2010).

[10]H. Peelaers and C. G. Van de Walle, "Brillouin zone and band structure of β-Ga$_2$O$_3$," Phys. Status Solidi B **252**, 828–832 (2015).

[11]C. Janowitz, V. Scherer, M. Mohamed, A. Krapf, H. Dwelk, R. Manzke, Z. Galazka, R. Uecker, K. Irmscher, R. Fornari, M. Michling, D. Schmeißer, J. R. Weber, J. B. Varley, and C. G. V. d. Walle, "Experimental electronic structure of In$_2$O$_3$ and Ga$_2$O$_3$," New J. Phys. **13**, 085014 (2011).

[12]B. Liu, M. Gu, and X. Liu, "Lattice dynamical, dielectric, and thermodynamic properties of β-Ga$_2$O$_3$ from first principles," Appl. Phys. Lett. **91**, 172102 (2007).

[13]C. Sturm, J. Furthmüller, F. Bechstedt, R. Schmidt-Grund, and M. Grundmann, "Dielectric tensor of monoclinic Ga$_2$O$_3$ single crystals in the spectral range 0.5–8.5 eV," APL Mater. **3**, 106106 (2015).

[14]K. Irmscher, Z. Galazka, M. Pietsch, R. Uecker, and R. Fornari, "Electrical properties of β-Ga$_2$O$_3$ single crystals grown by the Czochralski method," J. Appl. Phys. **110**, 063720 (2011).

[15]A. Parisini and R. Fornari, "Analysis of the scattering mechanisms controlling electron mobility in β-Ga$_2$O$_3$ crystals," Semicond. Sci. Technol. **31**, 035023 (2016).

[16]N. Ueda, H. Hosono, R. Waseda, and H. Kawazoe, "Anisotropy of electrical and optical properties in β-Ga$_2$O$_3$ single crystals," Appl. Phys. Lett. **71**, 933 (1997).

[17]P. Giannozzi, S. Baroni, N. Bonini, M. Calandra, R. Car, C. Cavazzoni, D. Ceresoli, G. L. Chiarotti, M. Cococcioni, I. Dabo, A. Dal Corso, S. de Gironcoli, S. Fabris, G. Fratesi, R. Gebauer, U. Gerstmann, C. Gougoussis, A. Kokalj, M. Lazzeri, L. Martin-Samos, N. Marzari, F. Mauri, R. Mazzarello, S. Paolini, A. Pasquarello, L. Paulatto, C. Sbraccia, S. Scandolo, G. Sclauzero, A. P. Seitsonen, A. Smogunov, P. Umari, and R. M. Wentzcovitch, "Quantum ESPRESSO: A modular and open-source software project for quantum simulations of materials," J. Phys.: Condens. Matter **21**, 395502 (2009).

[18]A. Kokalj, "Computer graphics and graphical user interfaces as tools in simulations of matter at the atomic scale," Comput. Mater. Sci. **28**, 155–168 (2003).

[19]A. A. Mostofi, J. R. Yates, Y.-S. Lee, I. Souza, D. Vanderbilt, and N. Marzari, "wannier90: A tool for obtaining maximally-localised Wannier functions," Comput. Phys. Commun. **178**, 685–699 (2008).

[20]S. Baroni, S. de Gironcoli, A. Dal Corso, and P. Giannozzi, "Phonons and related crystal properties from density-functional perturbation theory," Rev. Mod. Phys. **73**, 515–572 (2001).

[21]J. Noffsinger, F. Giustino, B. D. Malone, C.-H. Park, S. G. Louie, and M. L. Cohen, "EPW: A program for calculating the electron–phonon coupling using maximally localized Wannier functions," Comput. Phys. Commun. **181**, 2140–2148 (2010).

[22]F. Giustino, M. L. Cohen, and S. G. Louie, "Electron-phonon interaction using Wannier functions," Phys. Rev. B **76**, 165108 (2007).

[23]C. Verdi and F. Giustino, "Frohlich electron-phonon vertex from first principles," Phys. Rev. Lett. **115**, 176401 (2015).

[24]R. H. Lyddane, R. G. Sachs, and E. Teller, "On the polar vibrations of alkali halides," Phys. Rev. **59**, 673 (1941).

[25]C. J. Pickard and M. C. Payne, "Extrapolative approaches to Brillouin-zone integration," Phys. Rev. B **59**, 4685 (1999).

[26]D. Chattopadhyay and H. Queisser, "Electron scattering by ionized impurities in semiconductors," Rev. Mod. Phys. **53**, 745 (1981).

[27]D. Rode, "Low-field electron transport," Semicond. Semimetals **10**, 1–89 (1975).

[28]K. Ghosh and U. Singisetti, "Rode's iterative calculation of surface optical phonon scattering limited electron mobility in N-polar GaN devices," J. Appl. Phys. **117**, 065703 (2015).